Supporting information for

Solid Earth

Delamination in Tibet: Deriving constraints from the density of eclogite

Zhilin Ye [a,b], Dawei Fan [a,*], Bo Li [a,b], Qizhe Tang [c], Jingui Xu [d,*], Dongzhou Zhang [d], Wenge Zhou [a]

[a] *Key Laboratory of High-Temperature and High-Pressure Study of the Earth's Interior, Institute of Geochemistry, Chinese Academy of Sciences, Guiyang, Guizhou 550081, China*

[b] *University of Chinese Academy of Sciences, Beijing 100049, China*

[c] *School of Information Engineering, Huzhou University, Huzhou, Zhejiang 313000, China*

[d] *Hawaii Institute of Geophysics and Planetology, School of Ocean and Earth Science and Technology, University of Hawaii at Manoa, Honolulu, Hawaii 96822, USA*

* Corresponding authors.

E-mail addresses: fandawei@vip.gyig.ac.cn (D. Fan), xujingui@hawaii.edu (J. Xu)

Text S1-S3
Table S1-S3
Figure S1-S12

Text S1. Discussion on the effects of bulk modulus and its pressure derivate of minerals on density

To evaluate the effect of bulk modulus (K_{T0}) and its pressure derivate (K_{T0}'), we calculate the mineral density using K_{T0} and K_{T0}' in different experiments (Figure S3). The results show that the influence of K_{T0} on density is limited. Only when the ΔK_{T0} between the two experiments (Arimoto et al., 2015; Xu et al., 2019) is 20 GPa, the density difference of 0.27% will be generated at 140km (~4.2 GPa). Moreover, the results of density differences in this study are comparable to that of Milani et al. (2015). For omphacite, the density profiles from Xu et al. (2019) and Zhang et al. (2016) are the same, as well as the results of this study and Nishihara et al. (2003). In this case, the maximum density difference is only 0.3%. But for epidote, due to too large K_{T0} (~162 GPa) in Holland et al. (1996) experiment, the maximum density difference is ~0.6%-1.2%. The density results of epidote in this study are similar to those of Qin et al. (2016) and Gatta et al. (2011). The influence of K_{T0}' on density is limited, and only the values of K_{T0} with very large differences can have a conspicuous impact on density. Meanwhile, the influence of K_{T0} and K_{T0}' on mineral density is interactive.

Text S2. Discussion on the effects of thermal expansion of garnet on density

The effects of temperature on V_{T0} are expressed as follows:

$$V_{T0} = V_0 \, exp \int_{300}^{T} \alpha_T \mathrm{d}T$$

where $\alpha_T = \alpha_0+\alpha_1 T+\alpha_2 T^{-2}$ (Fei, 1995) is the volumetric thermal expansion at ambient pressure. Due to the limited experimental data, we fixed α_1 and α_2 as 0 in the fitting. We extrapolate beyond our data when discussing the density of eclogite during the delamination process in the latter part of this

paper. Therefore, we compare the thermal expansion of garnet and its effect on density in different studies. The results show that the thermal expansion varies greatly in different experiments, especially at high temperatures (Figure S4 (a)). Even if the experiments are under the same process (Multi Anvil apparatus) and over the same temperature range (300-1700K) (Arimoto et al., 2015; Zou et al., 2012), different results are obtained. Moreover, the thermal expansion is also influenced by mineral composition. Considering the influence of extrapolation, the densities of garnet in different experiments are also calculated (Figure S4(b)). The results of garnet in this study are comparable to those of Milani et al. (2015, 2017). However, the difference between the garnet density predicted in this study and in Arimoto et al. (2015) would consistently increase with higher temperature, which will finally reach 1% at 1250 K. In this study, we conducted high-pressure and high-temperature experiments in a single DAC chamber to avoid the errors caused by different experiments. The chemical composition, experimental method, temperature range are factors that need to be considered.

Text S2. Density profile along Cenozoic geothermal line

The density profiles of eclogite and peridotite along the Cenozoic geotherm are shown in Figure 6b. With an increase of 10 vol. % garnet, the density of eclogite increases by ~1.8%. The density of Tibetan eclogite in this study is 3.47-3.60 g/cm^3, which is approximately 7.6%-11.6% larger than that of the surrounding peridotite (3.23 g/cm^3) at ~60 km. The densities of eclogite increase by ~2.0% for high-Fe eclogite and ~1.4% for low-Fe eclogite. A comparison of the surrounding peridotite with eclogites of different iron contents eclogite shows that the density of high-Fe eclogite (3.58-3.73 g/cm^3) is 11%-15.5% denser and that of low-Fe eclogite (3.47-3.56 g/cm^3) is 7.3%-10.4% denser.

Text S3. Stokes' Law

The velocity of fragmented block is calculated using the Stockes'equation,

$$\eta = \frac{2r^2 g\left(\rho - \rho_0\right)}{9\upsilon} \tag{7}$$

where

η = absolute viscosity (poise)

r = radius of fragmented block (cm)

g = acceleration of fragmented block (cm·s^{-2})

ρ = density of fragmented block (g·cm^{-3})

ρ_0 = density of surrounding lithospheric mantle (g·cm^{-3})

υ = terminal velocity of fragmented block in surrounding lithospheric mantle (cm·s^{-2})

Table S1. Unit-cell parameters of garnet, omphacite, epidote at high pressures and high temperatures.

(a) Garnet

P (GPa)	*T* (K)	*a* (Å)	*V* (Å^3)
0.0001	300	11.612(2)	1565.8(4)
0.45(2)	300	11.602(1)	1561.6(3)
1.20(2)	300	11.589(1)	1556.5(2)
2.45(2)	300	11.560(1)	1545.0(2)

3.47(2)	300	11.537(1)	1535.4(1)
4.55(2)	300	11.515(1)	1526.8(2)
6.10(2)	300	11.483(1)	1514.2(2)
8.00(2)	300	11.445(1)	1499.3(3)
9.95(2)	300	11.409(1)	1485.2(1)
11.97(2)	300	11.371(1)	1470.1(4)
16.65(2)	300	11.294(1)	1440.6(2)
18.70(2)	300	11.261(2)	1427.8(4)
1.75(2)	400	11.586(1)	1555.4(1)
2.70(2)	400	11.566(1)	1547.1(1)
2.90(2)	400	11.559(1)	1544.3(2)
3.97(2)	400	11.536(1)	1535.0(2)
5.40(2)	400	11.507(1)	1523.8(1)
7.10(2)	400	11.475(1)	1510.6(1)
9.15(2)	400	11.433(1)	1494.5(1)
13.47(2)	400	11.354(1)	1463.7(1)
17.25(2)	400	11.291(1)	1439.6(2)
19.90(2)	400	11.249(2)	1423.6(4)
2.30(2)	500	11.585(1)	1554.8(2)
3.45(2)	500	11.556(1)	1543.3(2)
4.47(2)	500	11.535(1)	1534.9(1)
6.37(2)	500	11.499(1)	1520.6(2)
8.07(2)	500	11.467(1)	1507.7(1)
10.30(2)	500	11.424(1)	1490.8(2)
15.15(2)	500	11.335(1)	1456.4(1)
17.85(2)	500	11.293(1)	1440.3(3)
21.50(2)	500	11.232(1)	1416.9(3)
3.07(2)	600	11.577(1)	1551.7(1)
4.27(2)	600	11.553(1)	1541.8(2)
5.05(2)	600	11.534(1)	1534.5(2)
7.85(2)	600	11.479(1)	1512.5(2)
12.10(2)	600	11.398(1)	1480.7(2)
17.02(2)	600	11.315(1)	1448.6(2)
23.30(2)	600	11.212(1)	1409.3(2)
3.95(2)	700	11.569(1)	1548.3(2)
5.60(2)	700	11.535(1)	1534.6(2)
9.30(2)	700	11.461(1)	1505.4(1)
13.90(2)	700	11.376(1)	1472.3(1)
19.70(2)	700	11.281(1)	1435.1(2)
25.57(2)	700	11.190(1)	1401.2(2)

(b) Omphacite

P (GPa)	*T* (K)	*a* (Å)	*b* (Å)	*c* (Å)	*β* (°)	*V* (Å^3)
0.0001	300	9.593(5)	8.771(8)	5.257(1)	106.83(3)	423.3(4)
0.45(2)	300	9.518(4)	8.737(5)	5.252(2)	105.19(2)	421.5(3)
1.20(2)	300	9.503(3)	8.739(4)	5.239(1)	105.27(2)	419.7(3)
2.45(2)	300	9.488(3)	8.694(4)	5.220(1)	105.39(2)	415.1(3)
3.47(2)	300	9.451(4)	8.694(5)	5.207(1)	106.38(3)	412.6(3)
4.55(2)	300	9.444(4)	8.659(6)	5.193(2)	105.55(1)	409.1(3)
6.10(2)	300	9.443(3)	8.611(19)	5.179(1)	106.18(3)	404.4(9)
8.00(2)	300	9.410(3)	8.563(16)	5.159(1)	106.03(2)	399.5(8)
9.95(2)	300	9.380(6)	8.493(8)	5.135(3)	105.92(5)	393.4(6)
11.97(2)	300	9.345(3)	8.487(5)	5.103(1)	105.99(2)	389.1(3)
16.65(2)	300	9.276(3)	8.384(5)	5.061(1)	105.50(2)	379.3(3)
18.70(2)	300	9.284(4)	8.350(7)	5.040(3)	106.23(4)	375.1(4)
1.75(2)	400	9.490(6)	8.755(8)	5.235(3)	105.26(4)	419.6(5)
2.70(2)	400	9.537(4)	8.723(6)	5.217(4)	106.47(3)	416.2(4)
2.90(2)	400	9.478(3)	8.710(4)	5.217(2)	105.36(2)	415.3(2)
3.97(2)	400	9.450(3)	8.703(4)	5.201(1)	105.52(2)	412.2(2)
5.40(2)	400	9.448(4)	8.628(6)	5.185(2)	105.58(3)	407.1(4)
7.10(2)	400	9.425(3)	8.632(19)	5.172(2)	106.16(3)	404.2(9)
9.15(2)	400	9.390(3)	8.557(16)	5.141(1)	105.94(4)	397.2(8)
13.47(2)	400	9.322(3)	8.497(6)	5.093(2)	106.11(2)	387.6(3)
17.25(2)	400	9.237(3)	8.448(5)	5.057(1)	105.46(1)	379.0(3)
19.90(2)	400	9.212(5)	8.371(7)	5.033(2)	105.41(3)	374.2(4)
2.30(2)	500	9.486(7)	8.770(9)	5.231(3)	105.32(4)	419.7(6)
3.45(2)	500	9.475(3)	8.711(5)	5.214(1)	105.44(3)	414.9(3)
4.47(2)	500	9.481(6)	8.716(9)	5.200(3)	106.37(3)	412.3(6)
6.37(2)	500	9.438(4)	8.614(5)	5.178(2)	105.64(3)	405.5(3)
8.07(2)	500	9.410(4)	8.637(5)	5.158(1)	106.07(2)	402.9(3)
10.30(2)	500	9.378(2)	8.540(12)	5.129(1)	105.81(2)	395.2(6)
15.15(2)	500	9.320(4)	8.458(6)	5.080(2)	106.08(3)	384.8(4)
17.85(2)	500	9.277(3)	8.455(5)	5.056(1)	105.46(2)	380.3(3)
21.50(2)	500	9.254(5)	8.321(8)	5.026(1)	106.27(2)	371.5(5)
3.07(2)	600	9.520(4)	8.790(5)	5.224(1)	106.58(3)	419.0(3)
4.27(2)	600	9.467(4)	8.699(5)	5.211(1)	105.47(2)	415.6(3)
5.05(2)	600	9.483(3)	8.712(4)	5.197(1)	106.33(2)	412.0(3)
7.85(2)	600	9.411(6)	8.632(8)	5.167(2)	105.74(2)	404.0(5)
12.10(2)	600	9.345(4)	8.548(9)	5.116(2)	105.79(2)	393.3(5)
17.02(2)	600	9.301(2)	8.433(4)	5.066(1)	106.13(3)	381.7(2)
23.30(2)	600	9.176(2)	8.339(3)	5.011(1)	105.29(1)	369.2(4)
3.95(2)	700	9.468(3)	8.752(4)	5.218(1)	105.42(3)	416.8(3)
5.60(2)	700	9.480(7)	8.707(9)	5.196(3)	106.33(4)	411.6(6)
9.30(2)	700	9.407(3)	8.622(5)	5.151(1)	106.02(1)	401.5(3)
13.90(2)	700	9.348(4)	8.490(5)	5.104(2)	106.03(2)	389.3(3)
19.70(2)	700	9.241(4)	8.381(6)	5.054(1)	105.40(1)	377.4(3)
25.57(2)	700	9.156(4)	8.289(7)	4.993(2)	105.16(2)	365.7(4)

(c) Epidote

P (GPa)	*T* (K)	*a* (Å)	*b* (Å)	*c* (Å)	*β* (°)	*V* (Å^3)
0.0001	300	8.9045(1)	5.6205(3)	10.267(1)	116.18(2)	461.2(2)
0.45(2)	300	8.8918(5)	5.6361(4)	10.147(1)	115.38(3)	459.4(1)
1.20(2)	300	8.8746(5)	5.6258(3)	10.125(1)	115.25(3)	456.7(1)
2.45(2)	300	8.8445(5)	5.6093(3)	10.094(1)	115.32(3)	452.3(1)
3.47(2)	300	8.8211(5)	5.5964(3)	10.066(1)	115.63(3)	448.7(1)
4.55(2)	300	8.7977(5)	5.5857(3)	10.040(1)	115.55(3)	445.2(1)
6.10(2)	300	8.7579(5)	5.5695(3)	9.995(1)	115.42(4)	440.1(1)
8.00(2)	300	8.7170(5)	5.5527(3)	9.950(1)	115.41(4)	434.6(1)
9.95(2)	300	8.6684(4)	5.5025(4)	9.884(1)	115.41(3)	427.8(1)
11.97(2)	300	8.5382(5)	5.5304(3)	9.843(1)	116.19(3)	421.9(1)
16.65(2)	300	8.4567(5)	5.5098(3)	9.747(1)	115.50(3)	409.9(1)
18.70(2)	300	8.4174(5)	5.5016(4)	9.7101(1)	115.83(3)	404.7(1)
1.75(2)	400	8.8694(5)	5.6251(3)	10.123(1)	115.49(3)	456.6(1)
2.70(2)	400	8.8487(5)	5.6121(3)	10.100(1)	115.55(3)	453.3(1)
2.90(2)	400	8.8411(5)	5.6097(3)	10.093(1)	115.37(3)	452.3(1)
3.97(2)	400	8.8168(5)	5.5947(3)	10.061(1)	115.51(3)	448.6(1)
5.40(2)	400	8.7855(5)	5.5818(3)	10.029(1)	115.38(3)	444.3(1)
7.10(2)	400	8.7433(5)	5.5641(3)	9.980(1)	115.35(3)	438.6(1)
9.15(2)	400	8.7108(5)	5.5477(3)	9.933(1)	115.40(3)	431.8(1)
13.47(2)	400	8.5532(4)	5.5312(4)	9.811(1)	115.11(2)	419.2(1)
17.25(2)	400	8.5162(4)	5.5012(4)	9.741(1)	115.74(2)	409.2(1)
19.90(2)	400	8.4062(5)	5.4989(4)	9.696(1)	115.67(3)	402.4(1)
2.30(2)	500	8.8649(5)	5.6276(3)	10.119(1)	115.45(3)	456.7(1)
3.45(2)	500	8.8363(5)	5.6103(3)	10.082(1)	115.34(3)	452.3(1)
4.47(2)	500	8.8130(5)	5.5946(3)	10.055(1)	115.46(3)	448.7(1)
6.37(2)	500	8.7731(5)	5.5759(3)	10.011(1)	115.31(3)	442.7(1)
8.07(2)	500	8.7376(4)	5.5609(3)	9.965(1)	115.17(3)	437.1(1)
10.30(2)	500	8.6902(4)	5.5345(3)	9.913(1)	115.19(3)	429.5(1)
15.15(2)	500	8.5285(4)	5.5214(4)	9.793(1)	115.32(2)	415.7(1)
17.85(2)	500	8.4837(4)	5.5053(4)	9.736(1)	115.23(2)	408.3(1)
21.50(2)	500	8.4076(4)	5.4712(4)	9.667(1)	115.16(2)	399.2(1)
3.07(2)	600	8.8573(5)	5.6185(3)	10.106(1)	115.41(3)	455.4(1)
4.27(2)	600	8.8312(5)	5.6039(3)	10.076(1)	115.35(3)	451.6(1)
5.05(2)	600	8.8092(5)	5.5943(3)	10.053(1)	115.50(3)	447.2(1)
7.85(2)	600	8.7522(5)	5.5652(3)	9.981(1)	115.48(3)	438.9(1)
12.10(2)	600	8.5689(5)	5.5383(3)	9.880(1)	116.07(3)	425.4(1)
17.02(2)	600	8.4718(5)	5.5144(3)	9.768(1)	115.81(3)	411.8(1)
23.30(2)	600	8.3689(5)	5.4851(4)	9.500(1)	116.34(3)	395.3(1)
3.95(2)	700	8.8434(5)	5.6145(3)	10.089(1)	115.47(3)	452.3(1)
5.60(2)	700	8.8075(5)	5.5946(3)	10.052(1)	115.33(3)	447.7(1)
9.30(2)	700	8.7292(5)	5.5571(3)	9.962(1)	115.36(3)	435.1(1)
13.90(2)	700	8.5361(5)	5.5516(3)	9.8479(1)	116.03(3)	421.2(1)
19.70(2)	700	8.4382(5)	5.5055(3)	9.7327(1)	115.78(3)	404.3(1)
25.57(2)	700	8.3384(5)	5.4734(4)	9.4677(1)	116.35(3)	389.9(1)

Table S2. Thermal EoS parameters derived from the fitting of *P-V-T* data to the HT-BM3-EoS

Composition	V_0 (Å^3)	K_{T0} (GPa)	$K_{T}'_0$	α_0 (10^{-5} K^{-1})	$(\partial K_T/\partial T)_P$ (GPa/K)
Garnet	1565.8(4)	172(2)	3.6(2)		
($Prp_{21}Alm_{47}Grs_{31}Sps_1$)	1565.8(4)	171.4(8)	3.5(1)	2.86(9)	-0.010(3)
Omphacite	423.3(4)	124(2)	3.7(4)		
($Quad_{48}Jd_{45}Ae_7$)	423.3(4)	122(2)	4.1(3)	4.7(4)	-0.025(6)
Epidote	461.2(2)	122(1)	2.5(2)		
($Ca_{2.02}Fe_{0.75}Al_{2.32}Si_{0.16}[SiO_4][Si_2O_7]O(OH)$)	461.2(2)	122.7(6)	2.49(8)	4.7(1)	-0.029(2)

Table S3. Thermal EoS parameters derived from the BM3-EoS of garnet, omphacite, and epidote in this study compared with previous studies.

	Composition	V_0 (Å^3)	K_{T0} (GPa)	$K_{T'0}$	$(\partial K_T/\partial T)_P$ (GPa/K)	α_0 (10^{-5} K^{-1})		References
Garnet	$Prp_{21}Alm_{47}Grs_{31}Sps_1$	1565.8(4)	171.4(8)	3.5(1)	-0.010(3)	2.86(9)	XRD(SC)[a]	This study
	$Prp_{14}Alm_{62}Grs_{19}Adr_3Sps_2$	1564.9(1)	159.0(9)	5.0(2)	-0.010(4)	2.56(44)	XRD(SC)	(Xu et al., 2019)
	$Prp_{28}Alm_{38}Grs_{33}Sps_1$	1570.2(2)	162(1)	4.3(2)	-0.010(7)	3.53(35)	XRD(SC)	(Xu et al., 2019)
	$Prp_{68}Alm_{24}Gr_5Sp_1$		167(2)	4.4(1)	-0.0235(20)		BLS[b]	(Lu et al., 2013)
	$Prp_{26}Alm_{63}Grs_6Adr_5$	1542.43(11)	175(3)	3.7(7)			XRD(SC)	(Beyer et al., 2021)
	$Prp_2Alm_1Grs_{87}Adr_9$	1679.2	163.8(5)	3.9(2)			BLS	(Jiang et al., 2004)
	Prp_{100}	1499.9 (15)	170.7(30)	4.1^{fixed}	-0.024(13)	2.97(45)	XRD(ED)[c]	(Zou et al., 2012)
	Prp_{100}	1506.15(16)	163.7(1.7)	6.4		2.5(2)	XRD(SC)	(Milani et al., 2015)
	Alm_{100}	1533.52(10)	172.6(1.5)	5.8 (5)			XRD(SC)	(Milani et al. 2015)
	Alm_{100}	1531.05(7)	179(3)	4^{fixed}	-0.043(14)	2.6(5)	XRD(ED)	(Arimoto et al., 2015)
	Grs_{100}	1664.46(5)	166.57(17)	4.96 (7)		2.09(2)	XRD(SC)	(Milani et al., 2017)
	Sps_{100}	1564.96	172(4)	5.0(9)	-0.049(7)	2.46(54)	XRD(ED)	(Gréaux and Yamada, 2014)
	Adr_{100}	1754.05	158.0(1.5)	4^{fixed}	-0.020(3)	3.16(2)	XRD(PD)[d]	(Pavese et al., 2001)
Omphacite	$Quad_{48}Jd_{45}Ae_7$	423.3(4)	122(2)	4.1(3)	-0.025(6)	4.7(4)	XRD(SC)	This study
	$Quad_{72}Jd_{28}$	424.7(7)	117(4)	6.9(12)	-0.026(5)	2.7(3)	XRD(PD)	(Nishihara et al., 2003)
	$Di_{70.5}Jd_{29.5}$	429(1)	122(3)s	4.6(5)		2.7(8)	XRD(SC)/BLS	(Hao et al., 2019)
	$Quad_{57}Jd_{42}Ae_1$	422.3(1)	123.6(5)	4_{fixed}	-0.011(5)	2.8(3)	XRD(SC)	(Xu et al., 2019)
	$Quad_{53}Jd_{27}Ae_{20}$	426.0(2)	115(2)	4.9(4)	-0.009(6)	3.4(4)	XRD(SC)	(Xu et al., 2019)
	$Di_{51}Jd_{49}$	423.9(3)	116(2)	4.3(2)			XRD(SC)	(Zhang et al., 2016)
	$Di_{45}Jd_{55}$	421.43(4)	122(1)	5.1(3)			XRD(SC)	(Pandolfo et al., 2012a)
	$Di_{44}Jd_{56}$	421.04(7)	119(2)	5.7(6)		2.64(2)	XRD(SC)	(Pandolfo et al., 2012b)
Epidote	$Ca_{2.02}Fe_{0.75}Al_{2.32}Si_{0.16}(SiO_4)(Si_2O_7)O(OH)$	461.2(2)	122.7(6)	2.49(8)	-0.029(2)	4.7(1)	XRD(SC)	This study
	$Ca_2A1_2FeSi_3O_{12}(OH)$	459.9(3)	162(4)	4_{fixed}			XRD(PD)	(Holland et al., 1996)
	$Ca_{1.97}Fe_{0.84}\ Al_{2.15}(SiO_4)(Si_2O_7)O(OH)$	456.2(2)	133.1(7)	4_{fixed}	-0.004(1)	3.8(5)	XRD(SC)	(Li et al., 2020)
	$Ca_{1.85}Fe_{0.79}\ Al_{2.19}Ti_{0.05}Si_{3.03}O_{12}(OH)$	461.1(1)	115(2)	3.7(2)			XRD(SC)	(Qin et al., 2016)
	$Ca_{1.925}\ Fe_{0.745}Al_{2.265}Ti_{0.004}Si_{3.037}O_{12}(OH)$	458.8(1)	111(3)	7.6(7)		5.1(2)	XRD(PD)	(Gatta et al., 2011)
	$Ca_2Fe_{0.5}Al_{2.5}Si_3O_{12}(OH)$	463.8(6)	116(7)	7.8(8)			XRD(PD)	(Fan et al., 2014)

a: Single-crystal X-ray diffraction; b: Brillouin spectroscopy; c: Energy dispersive X-ray diffraction d: Powder X-ray diffraction

Quad: Ca-Mg-Fe pyroxene (Morimoto, 1988), Prp: Pyrope, Alm: Almandine, Grs: Grossular, Sps: Spessartine, Adr: Andradite, Jd: Jadeite, Ae: Aegirine, Di: Diopside.

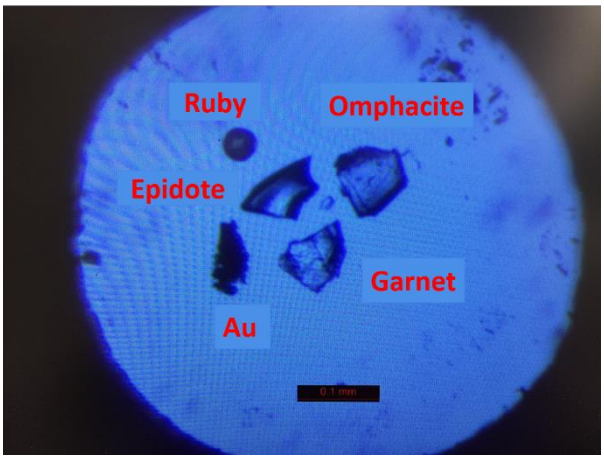

Figure S1. Representative sample chamber image showing garnet, omphacite, and epidote chips, together with Au and ruby sphere calibrant in Ne medium.

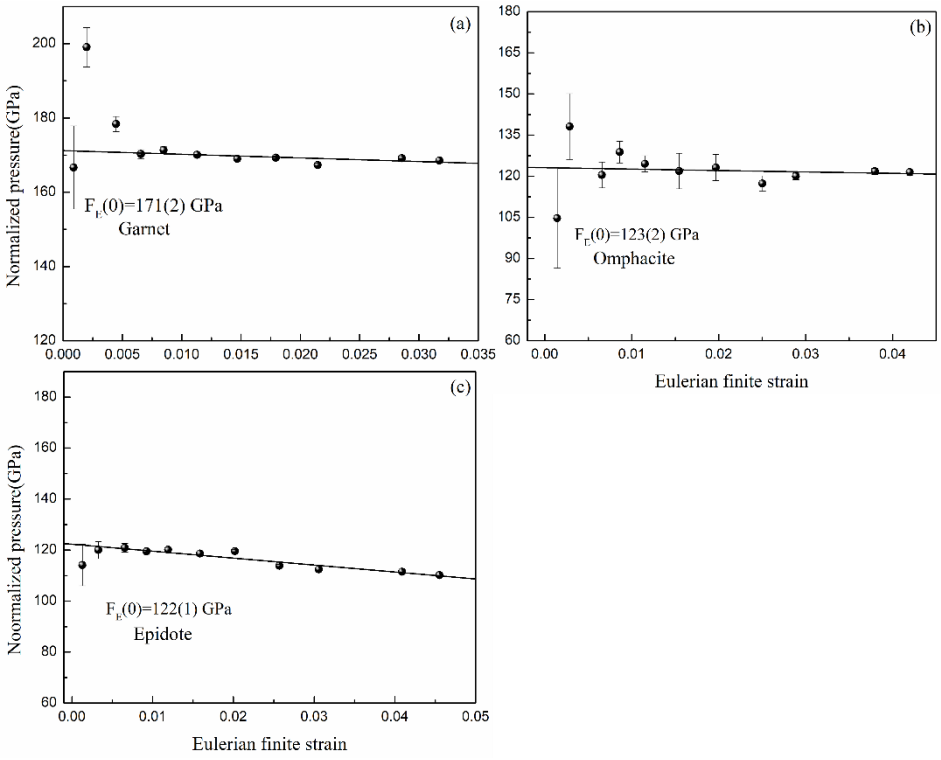

Figure S2. Eulerian finite stain-normalized pressure (F_E -f_E) plot of Garnet (a), Omphacite (b), and Epidote (c). The solid lines represent the linear fit through the data.

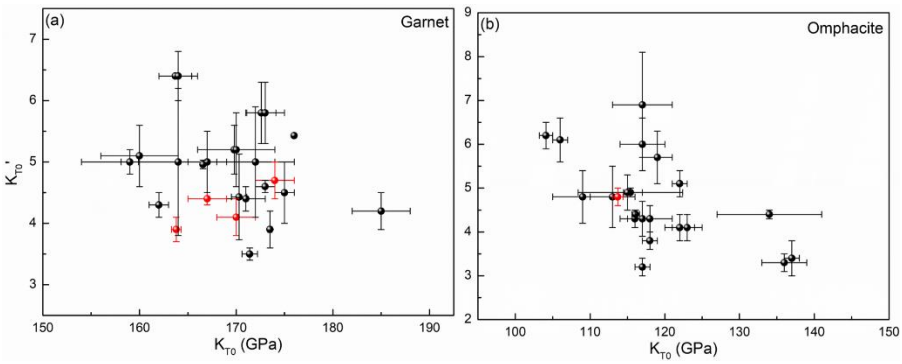

Figure S3. The isothermal bulk modulus (K_{T0}) and its pressure derivative (K_{T0}') plot of garnet (a) and omphacite (b). The red

solid circles represent the results of Brillouin light scattering. The adiabatic bulk moduli (K_{S0}) obtained with BLS are converted to K_{T0} by the relationship $K_{S0}= K_{T0}(1+\alpha\gamma T)$, where α is the thermal expansion, γ is the Grüneisen parameter, and T is the temperature.

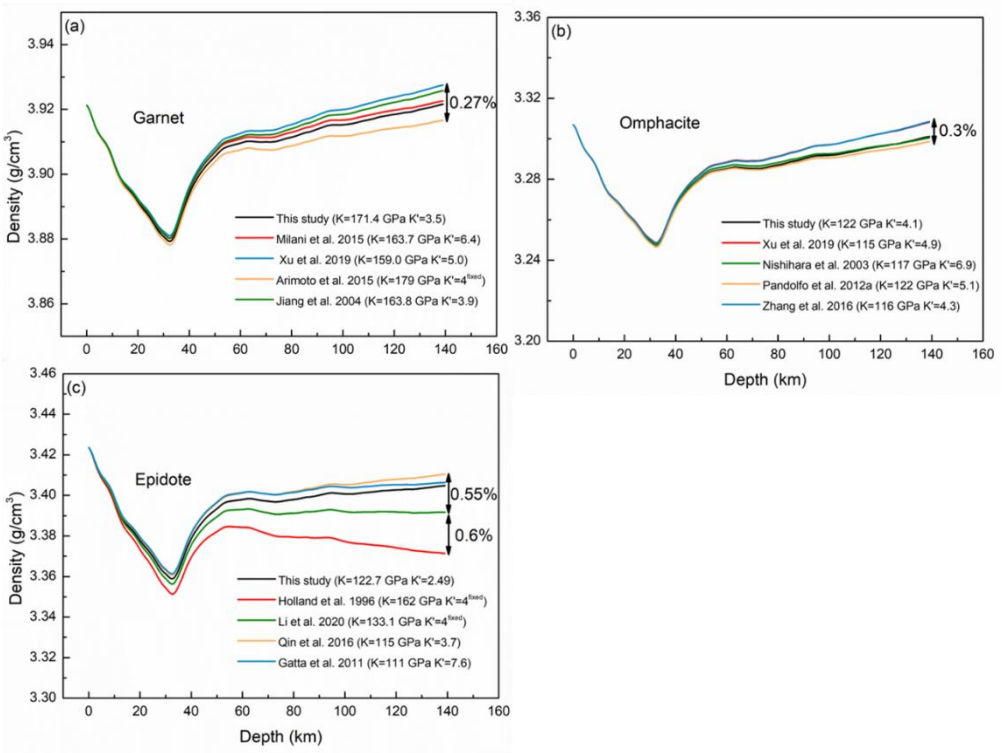

Figure S4. Density profiles of garnet (a), omphacite (b), and epidote (c) along with the Tibetan geothermal line. Different colored lines represent the calculated density profiles are derived from K_{T0} and K_{T0}'in different experiments, while other thermoelastic parameters are derived from this paper.

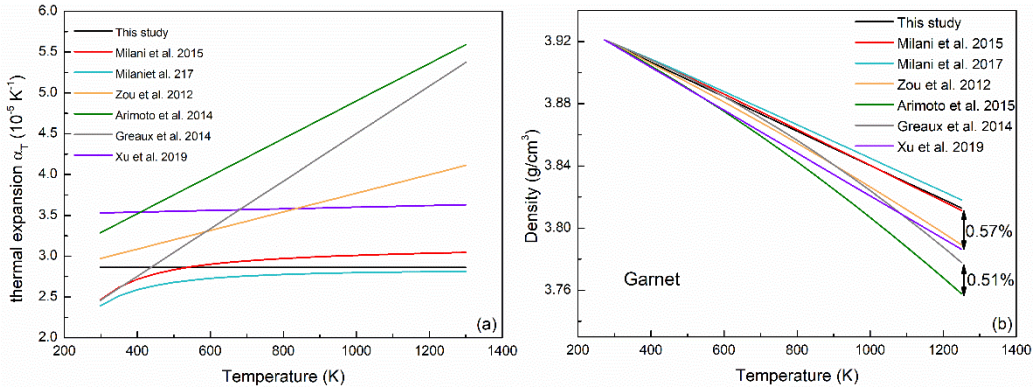

Figure S5. The evolution of garnet thermal expansion with temperature (a). Density profiles of garnet with different thermal expansion parameters under high temperature and room pressure (b).

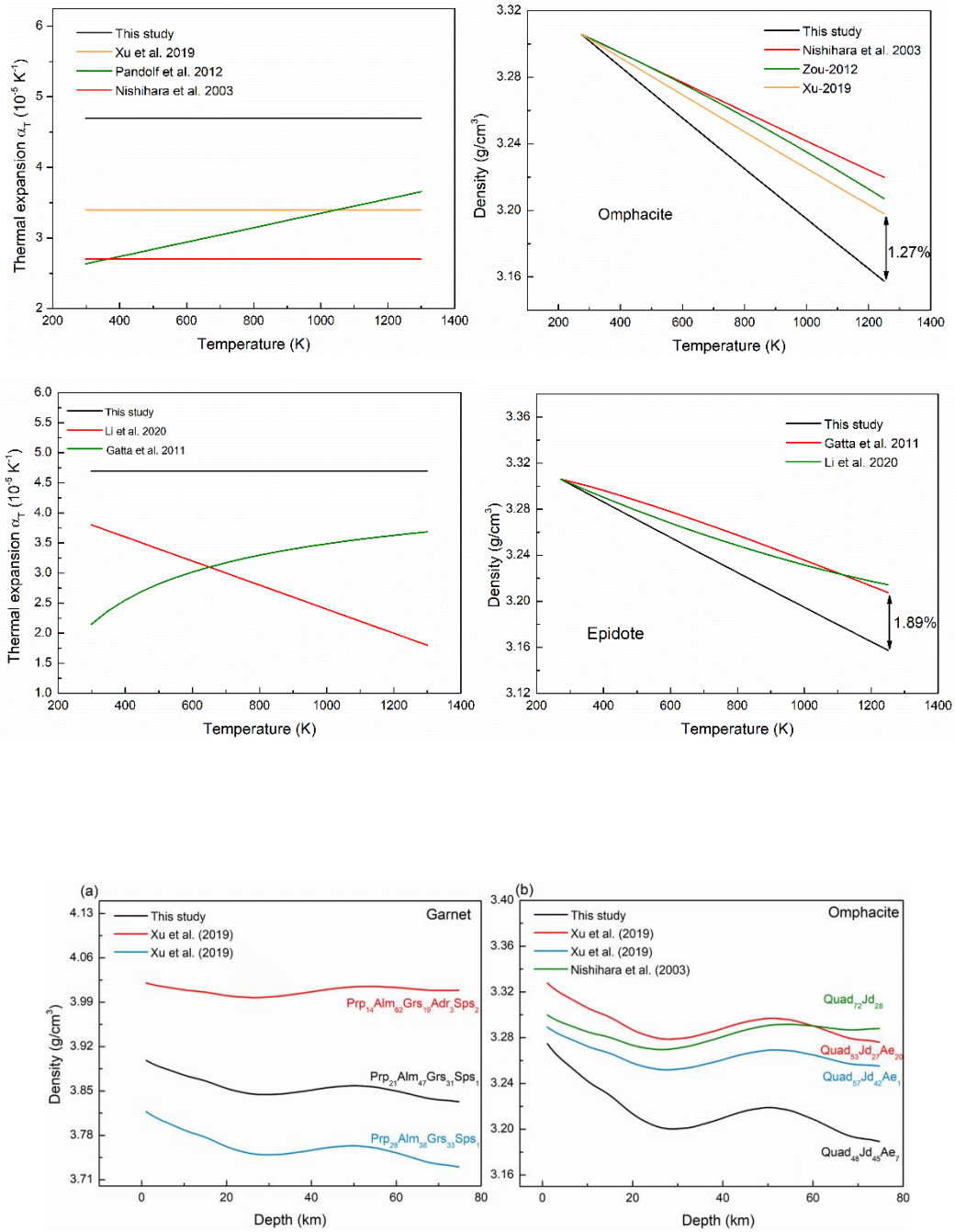

Figure S6. Density profiles of garnet (a) and omphacite (b) along the Cenozoic geothermal line. The garnets of $Prp_{14}Alm_{62}Grs_{19}Adr_3Sps_2$ and $Prp_{28}Alm_{38}Grs_{33}Sps_1$ are referred from Xu et al. (2019). The omphacites of $Quad_{53}Jd_{27}Ae_{20}$ and $Quad_{57}Jd_{42}Ae_1$ are from Xu et al. (2019) and $Quad_{72}Jd_{28}$ is from Nishihara et al. (2003).

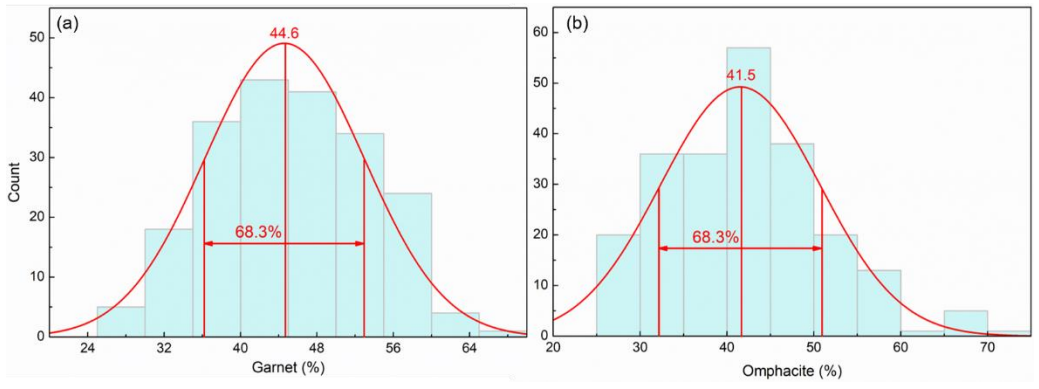

Figure S7. Normal distributions of garnet (a) and omphacite (b) content in eclogite from Tibet.

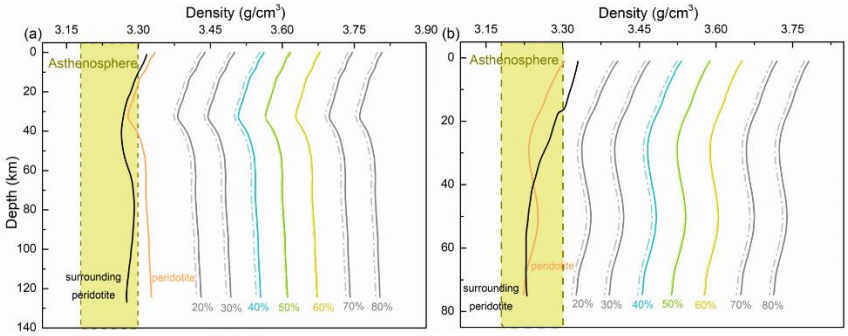

Figure S8. Density profiles of eclogite assemblages with and without epidote along the Paleozoic (a) and Cenozoic (b) geothermal lines. The solid line represents eclogite containing 5 vol. % epidote, while the dotted line indicates eclogite without epidote.

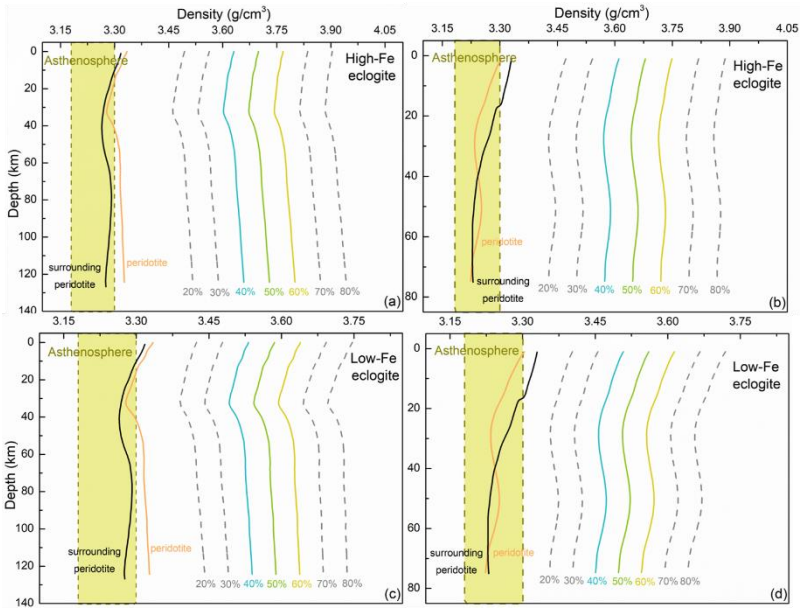

Figure S9. Density profiles of High-Fe and Low-Fe eclogite assemblages along the Paleozoic (a and c) and Cenozoic (b and d) geothermal lines. High-Fe eclogite is composed of $Prp_{14}Alm_{62}Grs_{19}Adr_3Sps_2$ and $Quad_{53}Jd_{27}Ae_{20}$, and Low-Fe eclogite is composed of $Prp_{28}Alm_{38}Grs_{33}Sps_1$ and $Quad_{57}Jd_{42}$ Ae_1 (Xu et al., 2019).

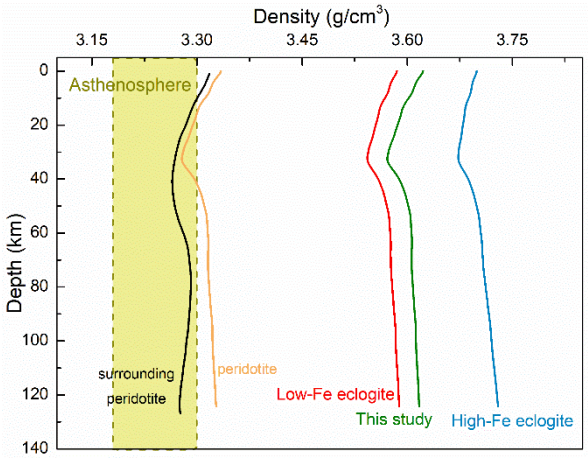

Figure S10. Density profiles of eclogite with different Fe contents with 50 vol. % garnet along the Paleozoic geothermal line.

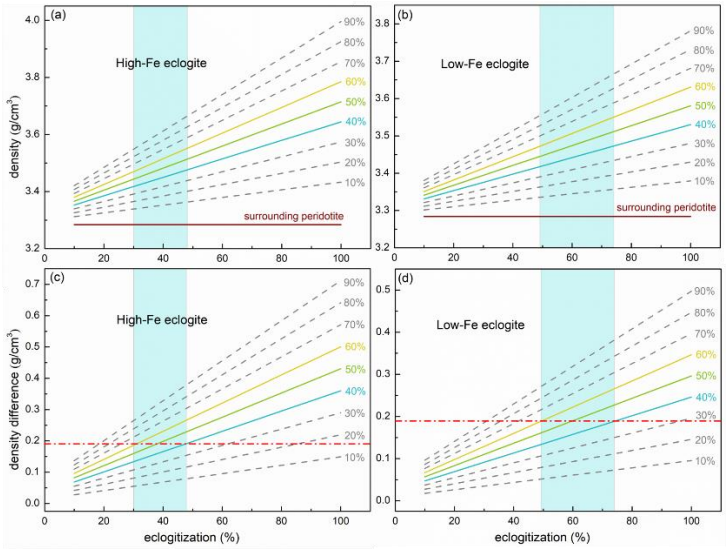

Figure S11. The effect of eclogitization on the density of subducted slab with high-Fe (a) and low-Fe (b) eclogite along the Paleozoic geothermal line. The rufous line represents the average density of the surrounding peridotite in this study. The blue shading indicates the possible degree of eclogitization. The density difference between high-Fe (c) and low-Fe (d) eclogite with different degrees of eclogitization and surrounding peridotite. The rufous line represents the average density of surrounding peridotite in this study. The blue shading indicates the possible degree of eclogitization.

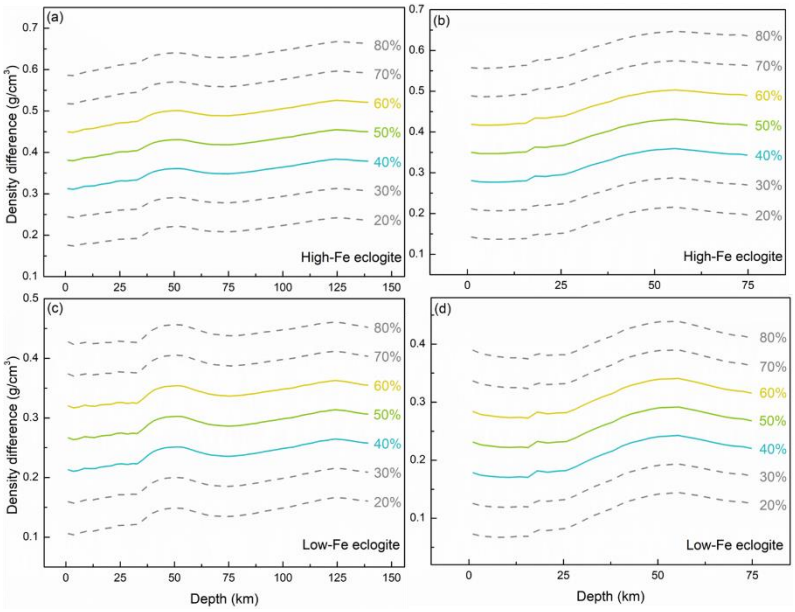

Figure S12. The density difference between High-Fe and Low-Fe eclogite assemblages and peridotite along the Paleozoic (a and c) and Cenozoic (b and d) geothermal lines, respectively.

References:

Arimoto, T., Gréaux, S., Irifune, T., Zhou, C. and Higo, Y.: Sound velocities of $Fe_3Al_2Si_3O_{12}$ almandine up to 19 GPa and 1700 K, Phys. Earth Planet. Inter., 246, 1–8, doi:10.1016/j.pepi.2015.06.004, 2015.

Beyer, C., Kurnosov, A. V., Ballaran, T. B. and Frost, D. J.: High-pressure and high-temperature single-crystal X-ray diffraction of complex garnet solid solutions up to 16 GPa and 823 K, Phys. Chem. Miner., 48(4), 17, doi:10.1007/s00269-021-01139-5, 2021.

Fan, D., Xu, J., Wei, S., Chen, Z. and Xie, H.: In-situ high-pressure synchrotron X-ray diffraction of natural epidote, Chin. J. High Press. Phys., 28, 257–261, doi:10.11858/gywlxb.2014.03.001, 2014.

Fei, Y.: Thermal Expansion, in Mineral Physics & Crystallography: A Handbook of Physical Constants, pp. 29–44., 1995.

Gatta, G. D., Merlini, M., Lee, Y. and Poli, S.: Behavior of epidote at high pressure and high temperature: a powder diffraction study up to 10 GPa and 1200 K, Phys. Chem. Miner., 38(6), 419–428, doi:10.1007/s00269-010-0415-y, 2011.

Gréaux, S. and Yamada, A.: P-V-T equation of state of $Mn_3Al_2Si_3O_{12}$ spessartine garnet, Phys. Chem. Miner., 41(2), 141–149, doi:10.1007/s00269-013-0632-2, 2014.
Hao, M., Zhang, J. S., Pierotti, C. E., Ren, Z. and Zhang, D.: High-Pressure Single-Crystal Elasticity and Thermal Equation of State of Omphacite and Their Implications for the Seismic Properties of Eclogite in the Earth's Interior, J. Geophys. Res. Solid Earth, 124(3), 2368–2377, doi:10.1029/2018JB016964, 2019.
Holland, T. J. B., Redfern, S. A. T. and Pawley, A. R.: Volume behavior of hydrous minerals at high pressure and temperature; II, Compressibilities of lawsonite, zoisite, clinozoisite, and epidote, Am. Mineral., 81(3–4), 341–348, doi:10.2138/am-1996-3-408, 1996.
Jiang, F., Speziale, S. and Duffy, T. S.: Single-crystal elasticity of grossular- and almandine-rich garnets to 11 GPa by Brillouin scattering, J. Geophys. Res. Solid Earth, 109(B10), doi:10.1029/2004JB003081, 2004.
Li, B., Xu, J., Zhang, D., ZhilinYe, Huang, S., Fan, D., Zhou, W. and Xie, H.: Thermoelasticity and stability of natural epidote at high pressure and high temperature: Implications for water transport during cold slab subduction, Geosci. Front., (January), doi:10.1016/j.gsf.2020.05.022, 2020.
Lu, C., Mao, Z., Lin, J., Zhuravlev, K. K., Tkachev, S. N. and Prakapenka, V. B.: Elasticity of single-crystal iron-bearing pyrope up to 20GPa and 750K, Earth Planet. Sci. Lett., 361, 134–142, doi:10.1016/j.epsl.2012.11.041, 2013.
Milani, S., Nestola, F., Alvaro, M., Pasqual, D., Mazzucchelli, M. L., Domeneghetti, M. C. and Geiger, C. A.: Diamond–garnet geobarometry: The role of garnet compressibility and expansivity, Lithos, 227, 140–147, doi:10.1016/j.lithos.2015.03.017, 2015.
Milani, S., Angel, R. J., Scandolo, L., Mazzucchelli, M. L., Ballaran, T. B., Klemme, S., Domeneghetti, M. C., Miletich, R., Scheidl, K. S., Derzsi, M., Tokár, K., Prencipe, M., Alvaro, M. and Nestola, F.: Thermo-elastic behavior of grossular garnet at high pressures and temperatures, Am. Mineral., 102(4), 851–859, doi:10.2138/am-2017-5855, 2017.
Morimoto, N.: Nomenclature of Pyroxenes, Mineral. Petrol., 39(1), 55–76, doi:10.1007/BF01226262, 1988.
Nishihara, Y., Takahashi, E., Matsukage, K. and Kikegawa, T.: Thermal equation of state of omphacite, Am. Mineral., 88(1), 80–86, doi:10.2138/am-2003-0110, 2003.
Pandolfo, F., Nestola, F., Cámara, F. and Domeneghetti, M. C.: High-pressure behavior of space group P2/n omphacite, Am. Mineral., 97(2–3), 407–414, doi:10.2138/am.2012.3928, 2012a.
Pandolfo, F., Nestola, F., Cámara, F. and Domeneghetti, M. C.: New thermoelastic parameters of natural C2/c omphacite, Phys. Chem. Miner., 39(4), 295–304, doi:10.1007/s00269-012-0484-1, 2012b.
Pavese, A., Diella, V., Pischedda, V., Merli, M., Bocchio, R. and Mezouar, M.: Pressure-volume-temperature equation of state of andradite and grossular, by high-pressure and -temperature powder diffraction, Phys. Chem. Miner., 28(4), 242–248, doi:10.1007/s002690000144, 2001.
Qin, F., Wu, X., Wang, Y., Fan, D., Qin, S., Yang, K., Townsend, J. P. and Jacobsen, S. D.: High-pressure behavior of natural single-crystal epidote and clinozoisite up to 40 GPa, Phys. Chem. Miner., 43(9), 649–659, doi:10.1007/s00269-016-0824-7, 2016.
Xu, J., Zhang, D., Fan, D., Dera, P. K., Shi, F. and Zhou, W.: Thermoelastic Properties of Eclogitic Garnets and Omphacites: Implications for Deep Subduction of Oceanic Crust and Density Anomalies in the Upper Mantle, Geophys. Res. Lett., 46(1), 179–188, doi:10.1029/2018GL081170, 2019.
Zhang, D., Hu, Y. and Dera, P. K.: Compressional behavior of omphacite to 47 GPa, Phys. Chem. Miner., 43(10), 707–715, doi:10.1007/s00269-016-0827-4, 2016.
Zou, Y., Gréaux, S., Irifune, T., Whitaker, M. L., Shinmei, T. and Higo, Y.: Thermal equation of state of $Mg_3Al_2Si_3O_{12}$ pyrope garnet up to 19 GPa and 1700 K, Phys. Chem. Miner., 39(7), 589–598, doi:10.1007/s00269-012-0514-z, 2012